Near-Field Coherent Radar Sensing Using a Massive MIMO Communication Testbed

Adham Sakhnini, Sibren De Bast, Mamoun Guenach, André Bourdoux, Hichem Sahli, Sofie Pollin

***Abstract*—This paper considers the problem of radar sensing by using a large number of antennas. We use the orthogonal frequency division multiplexing (OFDM) waveform, and show that the large arrays used in massive multiple-input multiple-output (MIMO) communications enable accurate localization in the array near-field, even at the narrow bandwidths typically encountered at low carrier frequencies. We validate our findings experimentally with a massive MIMO testbed operating at 3.5 GHz carrier frequency and 18 MHz OFDM bandwidth in an indoor environment. We consider a single moving cylinder, and demonstrate a median accuracy of (3.4, 5.6) cm in (x, y) in the near-field. We show that the accuracy is maintained with only a single subcarrier, and that the resolution increases with an order of magnitude when combining all antennas, effectively surpassing the 16.67 m bistatic range resolution set by the OFDM waveform. We use a radar symbol duration of 71.88 µs at an effective transmission period of 2.5 ms, which indicates that the radar and communication systems can be implemented in time-division with a capacity loss of only 2.9%. Our results suggest that near-field radar sensing can be integrated into future massive MIMO systems operating at low carrier frequencies and narrow bandwidths.**

***Index Terms*—Joint radar and communications, massive MIMO, near-field localization, experimental results.**

I. Introduction

As wireless communication systems are experiencing dramatic improvements in processing capabilities and bandwidths [1]–[4], it has been observed that the hardware is showing an increasing resemblance to that of modern radar systems. Combined with the increasing amount of allocated spectral resources, operating a radar system by reusing the same hardware has started to become feasible. This has attracted a considerable amount of interest under the umbrella of *joint radar (or sensing) and communications*, and recent works covering the topic are extensive, with several review papers being published only in the last few years [5]–[15]. Signal processing aspects are considered in [5], automotive applications in [6]–[8], mobile systems in [9], [10], and spectrum management and dual function systems in [11]–[15].

A recent technology is massive MIMO communications, which enjoys the advantages of increased power and spectral efficiencies by employing a large number of antennas at the base-station [16]. It is currently considered as a corner-stone in wireless technology, and has recently been introduced in the fifth generation of wireless communication standards [1], [17], while also serving as a strong candidate for supporting the massive connectivity in future industrial internet of things networks [18], [19].

In [17], the idea of using the same massive MIMO hardware for radar sensing was suggested, where it is envisioned that a further cross-fertilization between radar and communications theory will stimulate new and interesting progress in the respective fields. While these ideas are not strictly new in the context of MIMO systems (see e.g., [20]), the scale in the number of antennas appears to not have been previously considered in great detail. In [21], it is shown that for a sufficiently large number of antennas at the base station, a given detection performance can always be satisfied regardless of the interference statistics when using robust Wald-type detection, demonstrating the favorable interference rejection capabilities in massive MIMO radar systems.

In the context of communication-centric hardware reuse, most demonstrations have been carried out with a rather limited number of antennas. In the works [22]–[25], the 5G-NR waveform is utilized for simultaneous radar sensing. Self-interference cancellation schemes are considered in [22] in order to enable full-duplex operation in a 2.4 GHz transceiver, demonstrating simultaneous range-Doppler imaging during downlink transmission. In [23], a similar system is demonstrated at the 28 GHz band, using a single transmitter and receiver with mechanical scanning to map the environment. In [24], full-duplex transceivers are further highlighted as being key in enabling simultaneous radar sensing, demonstrating the functionalities in the 2.4 GHz and 28 GHz frequency bands, with the latter system also using mechanical steering to enable angular discrimination. In [25], a millimeter-wave setup is considered, wherein the radar and communication systems are jointly realized through time division multiplexing, where the main focus is enabling efficient scheduling schemes that jointly optimize the respective performances. The proposed system is validated using a 28 GHz communication system with a 64 antenna phased array, demonstrating both accurate ranging and high data rates. Furthermore, in [26], a 71-76 GHz transceiver with a fully digital waveform is demonstrated, using a single transmitter and receiver, where a competitive performance is obtained when compared with dedicated a 77 GHz radar module. Similar to [23], [24], angular discrimination was made available mechanically, by mounting the transmitter on a slider using a stepping motor.

While these recent works enable communications and radar sensing in the same device, experimental setups with massive MIMO arrays appear to yet be missing in the literature. To that end, and in contrast to previous works, we have in this paper reconfigured a massive MIMO testbed operating at the sub-6 GHz frequency bands for the purposes of radar sensing in an indoor environment, demonstrating accurate localization in the near-field of the antenna array, while using only a modest amount of time-frequency resources. The system employs the OFDM waveform, and the processing is done through the channel state information (CSI). Since our work is not only

 https://doi.org/10.1109/TWC.2022.3148035

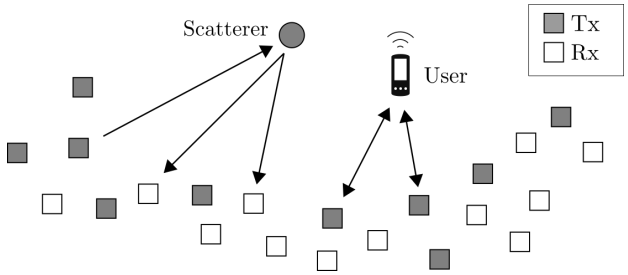

Figure 1: A scenario consisting of a dense and distributed system of antennas, used for both communications and radar sensing. This paper considers the radar functionality.

limited to co-located arrays, but also distributed arrays, we refer to a specific antenna synonymously as an access point (AP).

The scenario envisioned is motivated by recent works in distributed (or cell-free) massive MIMO communication systems [27], [28], consisting of a large number of spatially distributed APs. In the considered setup, we envision the simplest possible implementation of the radar functionality using time division duplexing with the primary communication system, and thereby circumventing the need for advanced joint transmission and co-processing schemes [29]. As shown in this paper, the incurred loss on the communication system is only nominal thanks to the short range scenario considered. Furthermore, we do not assume full-duplex transceivers as in e.g., [24], although it is advantageous whenever accessible (the models used can handle either case). Hence, at any given time instance, the APs are divided into sets of dedicated transmitters and receivers, as handled by a joint-radar and communications scheduler. It is assumed that the respective radar transmitters are orthogonal by some multiplexing (in e.g., time or frequency), so that the corresponding backscattered echoes can be isolated at the receivers. Since the APs are assumed to share the same fronthaul, the receivers know the transmitted data, and can hence use the waveform to extract information about the scattering environment. In the case of OFDM, this can be conveyed through the CSI, which is obtained after conventional demodulation and data removal [30], [31]. The benefit of this approach (over conventional radar correlation processing) is that the information extraction is compliant with existing OFDM standards, which implies that the signal processing blocks can be shared. Once the CSI is extracted, the system can be considered as an exclusive radar system, wherein conventional single-input single-output (SISO) radar processing can be carried out for any pair of transmitters and receivers, followed by a signal combining of all transmit-receive channels.

In contrast to traditional single-antenna systems (or small arrays), we recognize the task of combining the output of hundreds to thousands of spatially distributed antennas as the main challenge, but also the big opportunity of leveraging massive MIMO systems for radar applications. The challenges stem in the computational demands required for real-time processing, the possibly distributed nature of the antennas and hence the requirement to synchronize and calibrate the system, acquiring knowledge of the exact antenna locations, as well as properly scheduling the transmitters and receivers in order to strike a good balance between communications and radar performance. In order to limit the scope of this paper, we focus on the signal combining aspects.

Signal processing in multi-antenna systems has been studied for years in the radar community (see e.g., [20], [32], [33] for the distributed case, and [34]–[37] for the co-located case), where it is well known that spatially distributed arrays with large apertures provide high spatial resolution when processed coherently [32], [38]. However, we recognize some additional challenges inherent to the considered scheme, such as the scatterers residing in the near-field, being spatially extended, partially occluded and non-isotropic, as well as violating the typically imposed signal and array narrowband assumptions (for the latter, see e.g., [39]). All things considered, we find all these aspects difficult to model reliably, which motivates the use of real-world sensor data.

Compared to previous works in joint radar and communications, our focus is on near-field high resolution detection using a large number of antennas. Our contributions are as follows:

- We provide a signal model and a set of matched filter approximations for the considered OFDM MIMO system. The Cramér-Rao lower bound and the coherent ambiguity function is used to assess the system performance. We provide a system analysis, and a description of the data processing and system calibration methods used.
- We study the specific case of our massive MIMO hardware setup, and show numerically that sensing is enabled in the near-field. Our analysis reveals that a high degree of spatial resolution can be attained in the near-field of the array, even when the system operates with very low bandwidth. This is obtained when processing the MIMO channels coherently, and is made possible by the diversity in look-angles from the widely distributed antennas.
- We demonstrate a case of massive MIMO communications hardware re-use for the purposes of radar sensing. To the best of our knowledge, this has not been previously demonstrated.
- For a single moving cylinder that is located in the near-field of the array, we show that the resolution increases with over an order of magnitude when combining all of the transmit-receive channels, effectively surpassing the 16.67 m bistatic range resolution set by the 18 MHz OFDM bandwidth.
- In the considered scenario, we show that practically no bandwidth is required for localization as all of the performance gains can be attributed to the dense and spatially distributed array.

Our observations are well suited within the framework of massive MIMO communications, and are consistent with recent findings in wireless positioning, where it has been shown that the need for large signal bandwidths can be circumvented by processing a set of spatially distributed antennas coherently [40]. The results indicate that the massive MIMO paradigm may provide an opportunity for simultaneous radar sensing in the near-field, despite the narrow bandwidths typically

encountered at low carrier frequencies.

We structure this paper as follows. First, the signal model is presented, along with the system and signal assumptions made. The associated signal processing is then presented, where a set of matched filter approximations are introduced for processing the received data, along with some common radar performance metrics. The testbed is then presented in Section IV, and a numerical evaluation is provided in Section V. The experimental results are presented in Section VI.

II. Signal model

The scenario considered is illustrated in Fig 1, which considers a dense and distributed system of antennas, used for both communications and sensing. The system is operated with a shared fronthaul, where some antennas are allocated for transmission, and some for reception using a joint-radar and communications scheduler. The transmitters and receivers are denoted by the indices $m = 1 \dots M$ and $n = 1 \dots N$, and are located at the positions (x_m, y_m) and (x_n, y_n).

We assume that the transmitters and receivers operate in the same frequency band, with entirely digital architectures, and assume that the motion of any scatterer can be approximated as being linear over the observation period (the linearity assumption allows us to exclude high-order acceleration terms in the subsequent processing). No assumptions are made on the antenna positions, which in turn may be configured to have arbitrary geometries. Similarly, the scatterers may be in the near-field. The OFDM waveform is used, and the CSI is extracted after a cyclic prefix removal, followed by a fast Fourier transform which maps the signal into the frequency domain over the $k = 1 \dots K$ subcarriers (spaced at Δf Hz), and a data symbol removal (see e.g., [31] for details). The cyclic prefix implies no intersymbol interference, and the data is assumed known.

Since multiple transmitter and receivers are used, there is a total of MN paths per scatterer present. From a communications perspective, this may give rise to several advantageous effects such as favorable propagation and channel hardening [41]. In order to reap the same benefits of spatial diversity in the considered radar context, we assume that each of the individual transmit-receive paths are orthogonal (see e.g., [20], [35]). This implies that some sort of multiplexing scheme is used, such as time-division multiple access, wherein the receivers can recover the sum of echoes originating from each of the transmitters.

We let a coherent processing interval (CPI) consist of $l = 1 \dots L$ symbols that are transmitted every T_p seconds. Under the stated assumption, the received complex baseband signal at the n:th receiver, originating from the m:th transmitter and q:th path, can be well approximated as

$$x_{mnq}(k,l) = \alpha_{mnq} e^{-j2\pi(\frac{1}{\lambda}+\frac{\Delta f}{c}k)d_{mnq}} e^{-j2\pi\frac{T_p}{\lambda}l\dot{d}_{mnq}} \quad (1)$$

where α_{mnq} is a complex amplitude, which accounts for various losses. The distance d_{mnq} represents the length of the propagation path, and $\dot{d}_{mnq}$ represents the corresponding rate of change. As usual, c is the speed of light, and λ is the wavelength at the carrier frequency f_c.

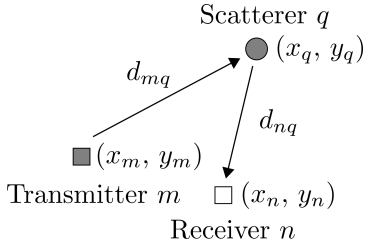

Figure 2: The single path scattering geometry for a single pair of transmitters and receivers.

Scattering geometry: Introducing the scattering geometry in Fig. 2, we let d_{mnq} represent the bistatic distance, which is expressed as

$$d_{mnq} = d_{mq} + d_{nq} \quad (2)$$

where d_{mq} is the distance between the m:th transmitter and q:th scatterer, and d_{nq} is the distance between the n:th receiver and q:th scatterer,

$$d_{mq} = \sqrt{(x_q - x_m)^2 + (y_q - y_m)^2} \quad (3)$$

$$d_{nq} = \sqrt{(x_q - x_n)^2 + (y_q - y_n)^2}. \quad (4)$$

Note that if the transmitters and receivers or co-located, then $d_{mq} \approx d_{nq}$. The corresponding range rates $\dot{d}_{mnq} = \dot{d}_{mq} + \dot{d}_{nq}$ are defined analogously by the respective time-derivatives as

$$\dot{d}_{mq} = \frac{x_m - x_q}{d_{mq}}\dot{x} + \frac{y_m - y_q}{d_{mq}}\dot{y} \quad (5)$$

$$\dot{d}_{nq} = \frac{x_n - x_q}{d_{nq}}\dot{x} + \frac{y_n - y_q}{d_{nq}}\dot{y} \quad (6)$$

where $\dot{x}$ and $\dot{y}$ is the velocity of the scatterer. Under the bistatic geometry, the complex signal amplitude is modeled as

$$\alpha_{mnq} = \beta\frac{\sqrt{G_{mq}G_{nq}}}{d_{mq}d_{nq}} \quad (7)$$

where G_{mq} and G_{nq} are the transmit and receive gains evaluated at the location of the q:th scatterer, and β contains any remaining factors, which include the transmit power, carrier frequency, radar cross section and various other system parameters. The model follows from the radar range equation, see e.g., [42], [43] for details.

Note that β is assumed constant for all transmit-receive pairs, which is an implicit and common assumption for coherent processing [32], [38]. However, this is not always a realistic assumption for extended and complex scatterers viewed from widely different aspect angles, since under such circumstances the scattering is in general not isotropic (see e.g., [33] for the unresolved case, and [44] which considers the related problem of source localization).

Note also that no assumptions have been made on the antenna geometry, and the model does not make any assumptions on whether the scatterers are in the far-field or not. If the antennas can be considered co-located and the scatterers in the far-field, then the model in (1) can be approximated to depend on the bistatic range, directions of arrival and departure. Similarly, the waveform is not assumed to be narrowband,

which implies that a certain scatterer may end up in different range-Doppler resolution cells for different pairs transmitters and receivers.

Additive noise model: Assuming superposition and additive noise, the recovered transmit-receive signals (for a set of Q scatterers) are expressed as

$$r_{mn}(k,l) = \sum_{q=1}^{Q} x_{mnq}(k,l) + \eta_{mn}(k,l) \tag{8}$$

where $\eta_{mn}(k,l)$ is some complex additive noise. Note that only the bistatic geometry in Fig. 2 has been taken into account, and that in general, $\eta_{mn}(k,l)$ is constituted from a mixture of multipath and interference components. For the sake of tractability, we assume that $\eta_{mn}(k,l) \in \mathcal{CN}(0, 2\sigma^2)$ is a white, zero mean and circularly symmetric Gaussian random variable with variance $2\sigma^2$.

Calibration model: To take calibration effects into account, we extend the signal model in (1) as

$$\begin{aligned}\tilde{x}_{mnq}(k,l) = \tilde{c}_{mn}\alpha_{mnq} e^{-j2\pi(\frac{1}{\lambda}+\frac{\Delta f}{c}k)(\tilde{d}_{mnq}-\Delta d^b_{mn})} \\ \times e^{-j2\pi\frac{T_p}{\lambda}l(\dot{d}_{mnq}-\Delta \dot{d}^b_{mn})}\end{aligned} \tag{9}$$

where $\tilde{c}_{mn}$ is a complex gain-phase offset, Δd^b_{mn} represents a range bias caused by timing offset, and where $\Delta \dot{d}^b_{mn}$ is a range-rate bias caused by a carrier frequency offset. The true distance $\tilde{d}_{mnq} = \tilde{d}_{mq} + \tilde{d}_{nq}$ is given by

$$\tilde{d}_{mq} = \sqrt{(x_q - \tilde{x}_m)^2 + (y_q - \tilde{y}_m)^2} \tag{10}$$

$$\tilde{d}_{nq} = \sqrt{(x_q - \tilde{x}_n)^2 + (y_q - \tilde{y}_n)^2} \tag{11}$$

where $\tilde{x}_m = x_m + \Delta x_m$, $\tilde{y}_m = y_m + \Delta y_m$, $\tilde{x}_n = x_n + \Delta x_n$ and $\tilde{y}_n = y_n + \Delta y_n$ are the true antenna locations, and x_m, y_m, x_n and y_n are the assumed antenna locations (which are used to construct the matched filterbanks in Section III-A), and Δx_m, Δy_m, Δx_n and Δy_n are the corresponding location errors, which are unknown.

III. Signal processing

A. Detection and estimation

In the following, we will consider the conventional matched filtering framework for both detection and estimation. This has the advantage of being computationally efficient, while also allowing for the most simple analysis. The processing proceeds by constructing a matched filterbank over a set of hypothetic scatterers under the assumed signal structure and geometry. The received data is matched against each of the scatterers, and if the output from a hypothesis exceeds a statistical threshold, the scatterer is deemed present (and otherwise rejected). As customary, we start by processing the signal in range and Doppler, followed by a combining of all transmit-receive channels (which is also known as the image formation or localization step).

1) Range-Doppler processing: The range profiles are obtained by matching the received returns at distances d along the subcarriers as

$$r^{(r)}_{mn}(d,l) = \frac{1}{K}\sum_{k=1}^{K} r_{mn}(k,l) f(d,k) \tag{12}$$

where $f(d,k) = w_f(k)e^{j2\pi\frac{\Delta f}{c}dk}$ is the matched filter, and $w_f(k)$ is some window function. A range-bin (or cell) corresponds to the output of $r^{(r)}_{mn}(d,l)$ at a given d. Similarly, the range-Doppler maps are evaluated as

$$r^{(rd)}_{mn}(d,\dot{d}) = \frac{1}{L}\sum_{l=1}^{L} r^{(r)}_{mn}(d,l) g(\dot{d},l) \tag{13}$$

where a given range bin d is matched at the corresponding range rate $\dot{d}$. A range-Doppler bin (or cell) corresponds to the output of $r^{(rd)}_{mn}(d,\dot{d})$ at a given d and $\dot{d}$. The matched filter is given by $g(\dot{d},l) = w_g(l)e^{j2\pi\frac{T_p}{\lambda}\dot{d}l}$, where $w_g(l)$ is some window function.

The purpose of the range-Doppler processing is two-fold. First, it provides a coherent processing gain, which in the ideal case is equal to KL. Second, it has the advantage of resolving scatterers in both range and Doppler, which allows clutter to be distinguished from moving objects [43]. When implemented with fast Fourier transforms, the computational complexity is $\mathcal{O}\left(MKL\log_2 KL\right)$ multiplications per receiving AP [45].

2) Coherent transmit-receive combining: Once the returns have been processed in range and Doppler, the processing proceeds by combining the transmit-receive channels to produce a spatial map of the environment. In the most straightforward approach, the transmit-receive channels are combined in both space and velocity, as

$$r^{(fb)}(x,y,\dot{x},\dot{y}) = \left|\sum_{m=1}^{M}\sum_{n=1}^{N} r^{(rd)}_{mn}(x,y,\dot{x},\dot{y})\overline{v}_{mn}(x,y)\right|^2 \tag{14}$$

where $r^{(rd)}_{mn}(x,y,\dot{x},\dot{y}) = r^{(rd)}_{mn}(d_{mn}(x,y), \dot{d}_{mn}(x,y,\dot{x},\dot{y}))$ is the range-Doppler map evaluated at a specific position-velocity cell, and $d_{mn}(x,y) = d_m(x,y) + d_n(x,y)$ is the bistatic distance and the $\dot{d}_{mn}(x,y,\dot{x},\dot{y})$ corresponding rate, following the geometry in Section II. The matched filter (or combining weights) are given by

$$\overline{v}_{mn}(x,y) = \frac{\sqrt{G_m(x,y)G_n(x,y)}}{d_m(x,y)d_n(x,y)} e^{j\frac{2\pi}{\lambda}d_{mn}(x,y)} \tag{15}$$

where $G_m(x,y)$ and $G_n(x,y)$ are the transmit and receive gains evaluated at the location x,y.

We call this method the *full backprojection*, and emphasize that for a given x, y, $\dot{x}$ and $\dot{y}$, the corresponding $d_{mn}(x,y)$ and $\dot{d}_{mn}(x,y,\dot{x},\dot{y})$ should be selected for each transmit-receive channel. In practice, since the range-Doppler maps are evaluated at discrete values (or bins), one may for a given x, y, $\dot{x}$ and $\dot{y}$ select the closest bin from $r^{(rd)}_{mn}(d,\dot{d})$ prior to matching, or take an interpolated value.

The full backprojection makes the most possible use of the assumed signal structure, and is therefore expected to provide

the best possible matched filtering performance. However, it has the drawback of requiring an evaluation over four dimensions, which for our purposes is computationally prohibitive. Since the primary task at hand is localization in space, the challenge resides in matching the velocity components $\dot{x}$ and $\dot{y}$ at low complexity. To that end, an alternative approach (which we call the *non-coherent backprojection*) proceeds by neglecting the Doppler-dependence altogether by non-coherently integrating the spatial images formed on a pulse-to-pulse basis from the range-profiles, as

$$r^{(ncb)}(x,y) = \frac{1}{L}\sum_{l=1}^{L}\left|\sum_{m=1}^{M}\sum_{n=1}^{N} r_{mn}^{(r)}(x,y,l)\overline{v}_{mn}(x,y))\right|^2 \tag{16}$$

where $r_{mn}^{(r)}(x,y,l) = r_{mn}^{(r)}(d_{mn}(x,y),l)$. The main difference from the full backprojection is that the four-dimensional matched filter is replaced by a two-dimensional matched filter, which is repeated L times. While computationally simpler, the method does not experience the same coherent processing gains, and does not use the Doppler dimension to resolve unknown scatterers (although, clutter can still be mitigated with slow-time filters, see e.g., [43]). A different approach approximates the received signal as being constant in the Doppler dimension. We call this approach the *constant Doppler backprojection*, and express it as

$$r^{(nb)}(x,y,\dot{d}) = \left|\sum_{m=1}^{M}\sum_{n=1}^{N} r_{mn}^{(rd)}(x,y,\dot{d})\overline{v}_{mn}(x,y)\right|^2 \tag{17}$$

where $r_{mn}^{(rd)}(x,y,\dot{d}) = r_{mn}^{(rd)}(d_{mn}(x,y),\dot{d})$. In this approximation, the signal is matched at the same range rate $\dot{d}$ over all pairs of transmitters and receivers, which is valid whenever the velocity of a scatterer is mapped to approximately the same velocity bin for all pairs of transmitters and receivers. By inspecting (5) and (6), it can be seen that this is a reasonable approximation when the array is sufficiently dense (or small), or when the scatterers move sufficiently slow, or are sufficiently far-away. The approximation is common in radar systems (see e.g., [39] and the references therein), and is suited for co-located arrays at relatively far distances from the scatterers. Under such circumstances, the combining step may also be well approximated to that of estimating the direction of arrival and departure of the scatterers, which is generally the preferred approach for localization. The main difference between (16) and (17) is that the former integrates the spatial images formed on symbol-by-symbol basis non-coherently, which has the advantage of making less assumptions on the mobility of the scatterers, whereas the latter method builds one spatial image from the combined range-Doppler maps at a fixed Doppler bin, which has the advantage of providing a coherent integration gain and suppression of clutter.

3) Self-interference and clutter rejection: To mitigate clutter and self-interference, we use mean subtraction in slow time, which cancels out lowpass Doppler components. This assumes that there is no carrier frequency offset between any pairs of transmitters and receivers, and that the clutter and self-interference components in the CSI are bandlimited around zero-Doppler. The clutter assumption is valid when the antennas are static, and the self-interference assumption is valid whenever the transmitters and receivers operate without any frequency offsets. We note that high-pass filtering in slow-time is a common operation in radar systems, see e.g., [42], [43].

B. Performance metrics

1) The Cramér-Rao lower bound (CRLB): We use the CRLB under the white Gaussian noise assumption as a conservative estimate on the localization accuracy. The bounds in x and y are given by the last two diagonal entries of the CRLB matrix, which is given as

$$\text{CRLB}(x,y) = \frac{1}{L}\left(\sum_{m=1}^{M}\sum_{n=1}^{N}\sum_{k=1}^{K}\boldsymbol{F}_{mnk}(x,y)\right)^{-1} \tag{18}$$

where $\boldsymbol{F}_{mnk}$ is the Fisher information coming from the k:th subcarrier originating the the m:th transmitter and n:th receiver. A derivation of $\text{CRLB}(x,y)$, along with the expression of $\boldsymbol{F}_{mnk}$ is provided in Appendix A.

2) The ambiguity function: For a set of Q stationary point scatterers, we define the spatial ambiguity function as the corresponding matched filter output, which is given by

$$\mathcal{A}(x,y) = \left|\sum_{q=1}^{Q}\sum_{m=1}^{M}\sum_{n=1}^{N}\sum_{k=1}^{K}\mathcal{A}_{mnkq}(x,y)\right|^2 \tag{19}$$

where

$$\mathcal{A}_{mnkq}(x,y) = e^{j2\pi\left(\frac{1}{\lambda}+\frac{\Delta f}{c}k\right)\Delta_{mnq}(x,y)} \tag{20}$$

and $\Delta_{mnq}(x,y) = d_{mn}(x,y) - d_{mnq}$. Note that usually $Q = 1$ is used in the literature, although this is not a restriction, see e.g., [32]. By using $\mathcal{A}(x,y)$, one may evaluate the spatial resolution and dynamic range of a given radar system by evaluating the beamwidth of the ambiguity response originating from a single test-scatterer.

3) SISO range-Doppler metrics: For additional analysis, it is also useful to consider the bistatic range and velocity dimensions separately. The respective resolutions are given by

$$\Delta d = \frac{c}{K\Delta f} \tag{21}$$

$$\Delta\dot{d} = \frac{\lambda}{LT_p} \tag{22}$$

and the maximum unambiguous bistatic range and velocity is given by

$$d_{max} = \frac{c}{\Delta f} \tag{23}$$

$$\dot{d}_{max} = \frac{\lambda}{2T_p} \tag{24}$$

which follows immediately from the sinusoidal model structure in equation (1), see e.g., [46] for details. Note that the metrics are constant and independent of the antenna or

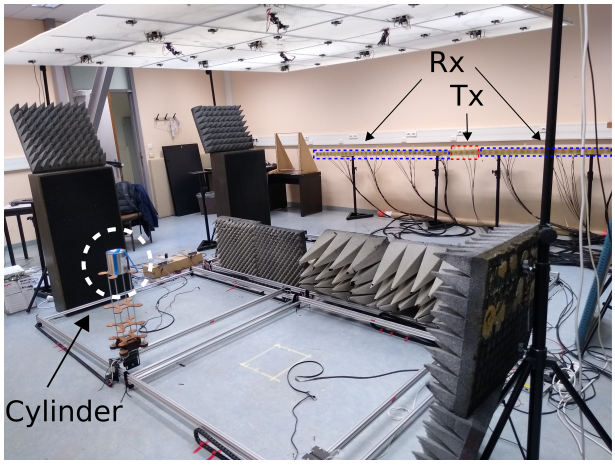

Figure 3: The massive MIMO testbed with absorbers mounted to shield from strong multipath reflections.

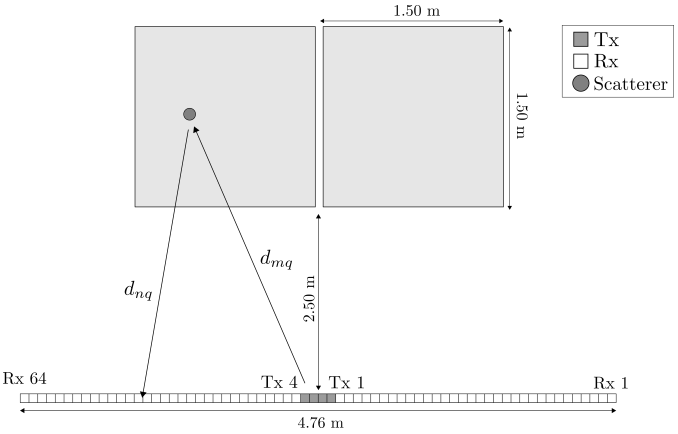

Figure 4: The geometry of the experimental setup in Fig. 3.

scatterer locations. The accuracy may be assessed by using the CRLB, which can be expressed as

$$\delta d_{mn} \approx \frac{\Delta d}{\sqrt{\pi \text{SNR}_{mn}}} \tag{25}$$

$$\delta \dot{d}_{mn} \approx \frac{\Delta \dot{d}}{\sqrt{\pi \text{SNR}_{mn}}} \tag{26}$$

for the case of temporally white additive Gaussian noise. The signal-to-noise ratio for a specific channel is defined as

$$\text{SNR}_{mn} = \frac{|\alpha_{mn}|^2 KL}{2\sigma^2} \tag{27}$$

where KL corresponds to the per-channel coherent processing gains after range-Doppler processing. For the sake of clarity, we have provided a derivation in Appendix A.

IV. The massive MIMO testbed

A. System setup

We use the 5G massive MIMO system developed by National Instruments (NI) as a distributed testbed to study the presented radar functionality. The testbed resides at the Department of Electrical Engineering (ESAT) at KU Leuven, and implements the OFDM waveform at mid-band under a 3GPP LTE-TDD like frame structure. In total, the testbed supports up to 128 antennas at the base station and 12 antennas at the user side [47]. The setup has previously been used for the purposes of positioning and communications [48]–[50].

Table I: Some system parameters and derived performance metrics used in the testbed.

System parameters	**Symbol**	**Value**	**Unit**
Carrier frequency	f_c	3.5	GHz
Carrier wavelength	λ	8.57	cm
Sampling rate		30.72	MHz
No. subcarriers	K	100	
Subcarrier spacing	Δf	180	kHz
Symbol bandwidth	$K\Delta f$	18	MHz
Cyclic prefix length	T_c	5.21	µs
Symbol duration	T_s	66.67	µs
OFDM modulation format		QPSK	
Radar parameters			
No. receivers	N	64	
No. transmitters	M	4	
Distance between antennas		0.07	m
No. symbols	L	640	
PRI duration	T_p	0.5	ms
CPI duration	LT_p	320	ms
SISO performance metrics			
Bistatic range resolution	Δd	16.67	m
Bistatic Doppler resolution	$\Delta \dot{d}$	1.34	m/s
Maximum unambiguous bistatic range	d_{max}	1667	m
Maximum unambiguous bistatic Doppler	$\pm \dot{d}_{max}$	85.7	m/s
CRLB in bistatic range at 20 dB SNR_{mn}	δd_{mn}	0.94	m
CRLB in bistatic Doppler at 20 dB SNR_{mn}	$\delta \dot{d}_{mn}$	0.08	m/s

The experimental setup is illustrated in Fig. 3, and the geometry in Fig. 4. Since the system does not implement simultaneous transmit and receive at the base station, we reconfigure the testbed to use the antennas at the base station as dedicated receivers, and the user terminal antennas as dedicated static transmitters, forming a distributed network of bistatic radar nodes. As inspired by the recent works in distributed massive MIMO communications, the elements are organized as a uniform linear array, reminiscent to that of the radio stripes architecture [27]. The system is configured to use $N = 64$ receiving, and $M = 4$ transmitting antennas (see [51] for details on the antennas), corresponding to a total of $MN = 256$ transmit-receive channels. This serves as a trade-off between the performance and the duration of each measurement, since the amount of data that can be recorded is limited by the on-board data storage.

We note that by the decorrelation criteria in [33], the array is considered widely separated despite being densely distributed (since the look-angles vary significantly between different portions of the array). One major drawback with the array structure is that it does not fully exploit the spatial diversity enabled by the MIMO array [20], [35]. For our purposes, this architecture was the simplest to work with. We recognize that by optimizing the deployment, substantial performance gains can be achieved than what is presented in this paper.

B. The radar frame structure

Some of the system parameters used are illustrated in Table I. We operate the system at $f_c = 3.5$ GHz to get the best

possible Doppler resolution, and configure the radar frame (or CPI) as follows. Based on the 3GPP-LTE standard, each OFDM symbol is constructed to consist of 1200 subcarriers with 15 kHz subcarrier spacing. This corresponds to a symbol duration of 66.7 μs, and a cyclic prefix of duration 5.21 μs is used. For our purposes of sensing, we use the non-precoded uplink pilots for localization, since the user terminals are used as dedicated transmitters. There is a total of $K = 100$ subcarriers in the pilots, spaced at $\Delta f = 180$ kHz subcarrier spacing, and interleaved in frequency (OFDMA) between the different transmitters (i.e., users). This enables transmit orthogonality, as each associated pilot can be isolated at the receivers. The pilots are transmitted every 7 symbols, corresponding to a PRI of $T_p = 0.5$ ms, and modulated using quadrature phase-shift keying (QPSK).

We let each radar frame consist of $L = 640$ symbols, corresponding to a CPI duration of 320 ms. For a given experiment, a total of 20000 symbols are transmitted over a period of 10 seconds, corresponding to 31 radar frames, or a total of $5.12 \cdot 10^6$ received symbols when counting over all 256 transmit-receive channels. The long CPI duration was chosen to isolate the slowly moving cylinder from the clutter in the Doppler domain. In practice, a smaller duration is sufficient, given that the scatterers move sufficiently fast. For further details on the massive MIMO system, we refer to [47].

C. System calibration

1) Carrier frequency offset compensation: Starting from the calibration model in (9), we assume that $\Delta \dot{d}^b_{mn} \approx 0$ by the shared clock distribution and carrier frequency offset compensation in the communications standard [47], [52].

2) Antenna position calibration: From (9) it is seen that the antenna positions are coupled with the gain-phase coefficients $\tilde{c}_{mn}$ and the timing-offsets Δd_{mn}. This implies that either parameter cannot be estimated without knowledge of the other. For our purposes, we assume the antenna locations to be known by manually measuring the respective locations in Fig. 3 with respect to the positioning table. While very precise estimates are generally required for coherent processing, this was deemed sufficient for our setup.

3) Timing synchronization: An initial timing synchronization can be obtained through the shared clock synchronization distribution in the testbed. This synchronizes the transmitters and receivers sufficiently well for communications. However, for the purposes of radar, we found that errors in the order of meters were still present. To compensate for the residual errors, a reference scatterer with at least one known location is required estimate the range residual offsets $\Delta \hat{d}^b_{mn}$. Following (9), this is done by subtracting an estimated range (using the matched filter) with the true range. The range-bias is then compensated for by multiplying the k:th subcarrier with $e^{-j2\pi \frac{\Delta f}{c} \Delta \hat{d}^b_{mn} k}$ prior to range-processing.

4) Array gain-phase calibration: The deviations in gain and phase are modeled through $\tilde{c}_{mn}$ in (9), and are typically caused by non-ideal front-ends. We model these as being diagonal along the transmitters and receivers. Since $\tilde{c}_{mn}$ is multiplicative with β for a given scatterer (see (9) and (7)), we estimate the $\beta \tilde{c}_{mn}$ jointly by assuming a set of Q_{cal} known calibration points. This calibrates the system up to a scaling factor by compensating each transmit-receive channel prior to combining. After measuring out the antenna locations and compensating for carrier frequency and timing offsets, $\beta \tilde{c}_{mn}$ is estimated by the least squares formulation

$$\min_{\beta \tilde{c}_{mn}} \sum_{q=1}^{Q_{cal}} \sum_{l=1}^{L} \sum_{k=1}^{K} |\hat{r}_{mnq}(k,l) - \beta \tilde{c}_{mn} f_{mnq}(k,l)|^2 \qquad (28)$$

where $\hat{r}_{mnq}(k,l)$ is the calibration data from the q:th snapshots, $f_{mnq}(k,l) = \frac{1}{\beta} x_{mnq}(k,l)$ is the assumed signal model, and where we have assumed that β is approximately constant for each snapshot. The solution is given by

$$\beta \tilde{c}_{mn} = \frac{1}{Q_{cal}} \sum_{q=1}^{Q_{cal}} \frac{d_{mq} d_{nq}}{\sqrt{G_{mq} G_{nq}}} \hat{r}^{(rd)}_{mnq} e^{j \frac{2\pi}{\lambda} d_{mnq}} \qquad (29)$$

where $r^{(rd)}_{mnq}$ is the range-Doppler from (13) output evaluated at the assumed location and velocity.

D. Data preprocessing

After completing a measurement, the CSI is loaded off the testbed and stored for offline processing. Due to the large amount of data collected, the CSI is compressed by downsampling along the subcarriers and in slow-time. This is motivated by the complex sinusoidal structure in the signal model in (1), where the ranges and velocities are translated to frequency shifts in the respective dimension. After downsampling, the maximum unambiguous range and velocity is reduced by the corresponding downsampling factor. The procedure has the advantages of providing a coherent processing gain, which increases the SNR, as well as reducing the memory footprint and computational burden in the subsequent processing steps.

V. Numerical performance analysis

We proceed to study the performance numerically. First, we present some SISO performance metrics, and then proceed with an analysis when the channels are combined coherently.

A. SISO performance

Starting with the SISO performance, the metrics presented in Section III-B are shown in Table I. Using (23), we estimate a bistatic range resolution of 16.67 m. By comparing with the experimental setup in Fig. 3, the resolution implies that the entire setup is mapped into the first range resolution cell. Accordingly, the task of localization entails resolving multiple scatterers using the remaining slow-time and antenna dimensions. Using (22), the resolution in bistatic Doppler is estimated at 1.34 m/s, which is deemed sufficient to isolate most moving scatterers from static clutter. However, if windowing is used, the resolution typically degrades by approximately a factor of two, depending on the type of window used [53].

The maximum unambiguous bistatic range and Doppler velocity is estimated at 1667 m and 85.7 m/s. Since the experimental setup is in the orders of a few meters and located indoors, it is recognized that the received data is

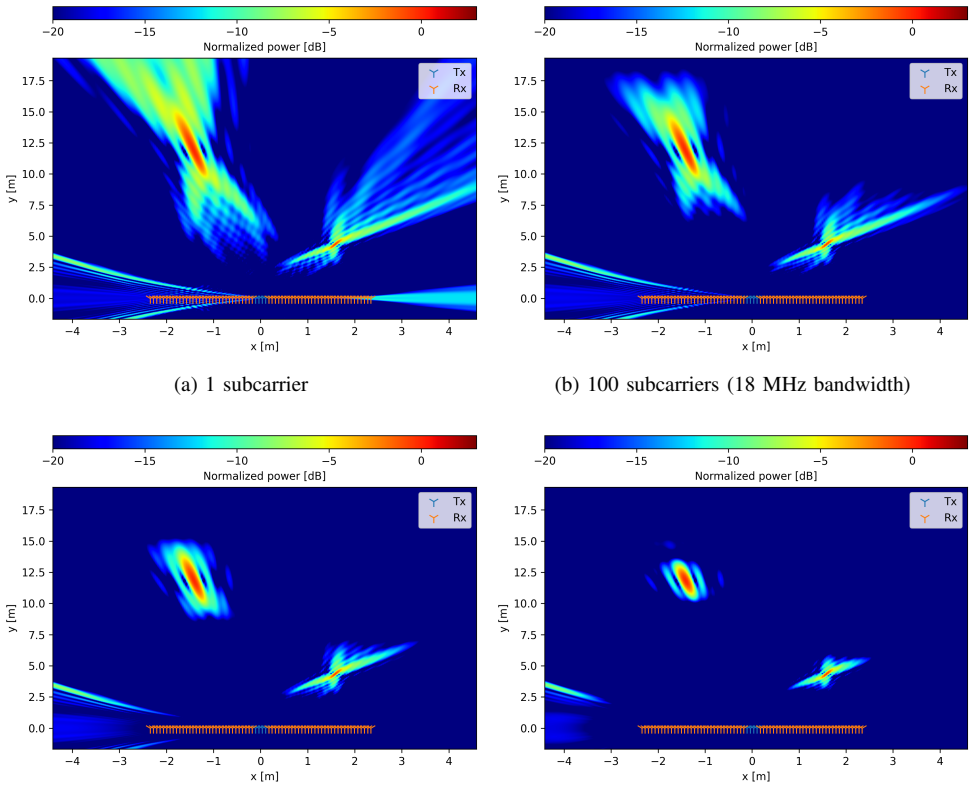

(a) 1 subcarrier

(b) 100 subcarriers (18 MHz bandwidth)

(c) 200 subcarriers (36 MHz bandwidth)

(d) 400 subcarriers (72 MHz bandwidth)

Figure 5: The spatial ambiguity function (19) for two scatterers located at $(x, y) = (1.6, 4.3)$ and $(x, y) = (-1.4, 11.8)$, illustrating the effect of the signal bandwidth. At close distances, the array resolution gain dominates, whereas at longer distances the signal bandwidth becomes significant. However, increasing the bandwidth increases the dynamic range as indicated by the reduction in the skirts around the main lobes.

very redundant and that one may downsample the CSI by an order of magnitude in the respective dimensions without any substantial loss in information, as mentioned in Section IV-D.

To evaluate the accuracy in bistatic range and velocity, we use a SNR of 20 dB after including all coherent processing gains, using (27). We measure a lower bound of 0.94 m in bistatic range using (25), and 0.08 m/s in bistatic velocity using (26).

B. MIMO performance

We proceed to evaluate the performance after coherently combining the transmit-receive channels, using the ambiguity function and the CRLB presented in Section III-B.

The ambiguity function for the considered system is illustrated in Fig. 5b). We consider two scatterers, with one being close to the array and the other being further away. It is observed that the scatterers are entirely resolved in x and y, effectively surpassing the resolution set by the bandwidth of the OFDM symbols. In order to further investigate the role of the bandwidth, we have also included the ambiguity functions for the cases when 1, 200 and 400 subcarriers are used with the same subcarrier spacing, corresponding to 0, 36 and 72 MHz bandwidth, as shown in Fig. 5a), c), and d). It is observed that at close distances, the array resolution gain dominates, whereas bandwidth contribution becomes substantial only further away from the array. Accordingly, for the short range scenario considered in Fig. 3, the array is expected to be the main contributing source of performance. However, despite the gain in resolution, a relatively poor dynamic range is observed as indicated by the wide skirts around the main lobes. This may mask scatterers when the environments are dense. It is observed that increasing the bandwidth also increases the dynamic range as indicated by the reduction in the skirts around the main lobes, which in turn may help resolve multiple scatterers.

To get an estimate of the localization accuracy after coherently combining the channels, we evaluate the CRLB in (18) with respect to the OFDM bandwidth. The scenario with the two point scatterers in Fig. 5 is considered, and for all bandwidths, we fix $\mathrm{SNR}_{mn} = 20$ dB. The bounds in x and y are illustrated in Fig. 6 for the respective scatterers. As can be seen, the CRLB lower-bounds the performance at sub-centimeter level accuracy for almost all bandwidths, indicating that very accurate localization is possible. By looking at the gain in performance when increasing the bandwidth, it can be seen that the improvement is only nominal for small bandwidths, until reaching a breaking-point where the bandwidth starts contributing substantially. For the scatterer located close

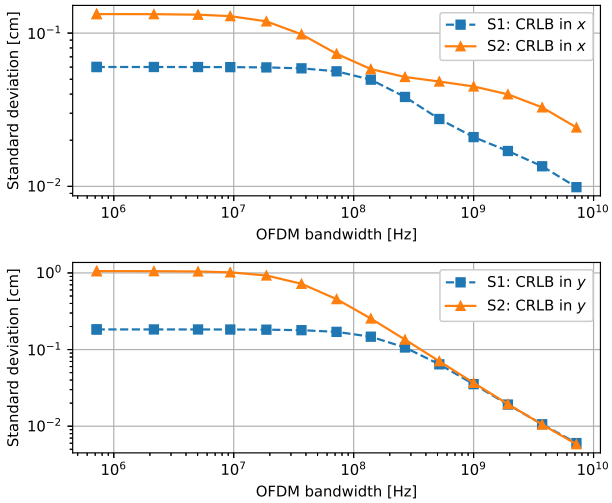

Figure 6: The CRLB in x and y with respect to the OFDM bandwidth, evaluated for the scatterers in Fig. 5 at fixed $\text{SNR}_{mn} = 20$ dB. The scatterers are located at S1: $(x, y) = (1.6, 4.3)$, S2: $(x, y) = (-1.4, 11.8)$.

to the array (S1), the breaking point starts at around 100 MHz, whereas for the scatterer further away (S2), it starts at around 10 MHz. Similarly to the results in Fig. 5, this indicates that the array resolution gain dominates the performance close the the array, whereas the bandwidth becomes more significant only further away. Intuitively, this is because the aspect angles along the array varies more the closer a scatterer is to the center of the array. Interestingly, since the testbed only uses a bandwidth of 18 MHz, the gain in accuracy at a fixed SNR is negligible when compared to using no bandwidth at all.

The analysis indicates that the massive MIMO testbed may be re-configured for radar sensing in the near-field, despite the poor range-resolution. This is enabled by the large accuracy and resolution gains which are obtained by coherently combining the large number of distributed antennas in the near-field. Interestingly, the bandwidth contribution is only substantial when large (i.e., $\gg$ 100MHz), or when the scatterers are located further away from the array (cf. Fig. 3).

VI. Experimental results

We proceed to demonstrate the massive MIMO testbed as a radar system in a short-range and near-field scenario. The experimental setup is illustrated in Fig. 3, and the scattering geometry in Fig. 4. We use a metallic cylinder to resemble that of an ideal isotropic point scatterer, and mount radio frequency (RF) absorbers around key reflectors in order to shield from strong multipath components during calibration. The cylinder is mounted on a positioning table which allows for precise positioning and measurement of ground truth locations. The experiments were carried out both with, and without RF absorbers, using the frame structure described in Section IV. In total, 760 radar frames were collected with RF absorbers, and 248 without, corresponding to approximately 125 and 41 million OFDM symbols when counted over all pairs of transmitters and receivers.

After acquisition, the samples were moved to an external memory, downsampled by a factor of five along the subcarriers and symbols, and then stored for offline processing, as described in Section IV-D. For this scheme, the downsampling provides a compression factor of 25, and a processing gain of approximately $10 \log_{10} 25 = 14$ dB. It is worth mentioning that if the SNR losses can be compensated, the same performance as presented can be obtained by transmitting only 20 subcarriers at a spacing of 900 kHz every 2.5 ms.

The system was calibrated following the procedure in Section IV-C. Timing offsets were estimated by comparing the true cylinder locations obtained from the positioning table with those measured, using an average of all measurements with RF absorbers. The sensor locations were measured out manually relative to the positioning table, and a set of five frames were taken from the upper right portion of Fig. 4 in order to calibrate the relative gain and phase offsets between the transmit-receive channels. We found that the best calibration was obtained when using the constant Doppler backprojection in (17).

In the signal processing, the bistatic range-profiles were evaluated over a total of 128 range-bins (after downsampling), corresponding to a cell-size of 2.6 m. The bistatic Doppler-profiles were similarly evaluated over 128 bins, giving a cell-size of 0.67 m/s. Since the study focused on resolving a single scatterer, no windowing was used unless otherwise mentioned. The gains in (15) where set as $G_m(x, y) = G_n(x, y) = 1$, and the spatial maps were formed over a cell-resolution of 4.2 cm in x and 3.7 cm in y for a total of 192×192 pixels. For the constant Doppler backprojection, the best performance was obtained when selecting the Doppler bin corresponding to the largest peak in the averaged range-Doppler map (over all SISO channels).

Since only a single scatterer is considered, the performance is analyzed by directly taking the largest component after the matched filter outputs. For the general case of multiple scatterers, one may consult the literature on radar detection theory [43]. However, we emphasize that the results presented, in particular the resolutions derived from the ambiguity and point spread functions, are also valid for multiple targets. For a particular image output, we divide the power of the scatterer with the median of the magnitude squared image as a rough measure of the SNR. Detections are kept if the transmit-receive channel with the smallest SNR in range-Doppler exceeds a 10 dB threshold. Since the processing relies on the Doppler dimension to isolate the cylinder from the clutter returns, some frames are lost whenever the cylinder makes corner turns and end up close to the zero Doppler bin. These missed detections are treated as outliers, and the results were accordingly trimmed by iteratively removing samples at five standard deviations from the mean in order to provide a realistic performance estimate.

The experimental results are organized as follows. First, we discuss two range-Doppler maps obtained from SISO processing. Then, we present the experimental matched filter outputs, and the localization performance obtained when coherently combining all the channels. The effect of reducing the OFDM bandwidth is then demonstrated, followed by an evaluation of the performance with respect to the number of antennas used.

A. Range-Doppler maps

Fig. 7 illustrates two range-Doppler maps before timing-offset compensation, as obtained using (13). The data originates from the first transmitter, measured at the right-most receiver in a), and the left-most receiver in b), each corresponding to Tx1, Rx1 and Rx64 in Fig. 4. The cylinder is located at the left part of the positioning table in Fig. 4, and moves diagonally from the upper right to the lower left corner. A Hanning window was applied in slow-time, and clutter and self-interference was removed by mean subtraction following the procedure in Section III-A.

As can be seen from the images, the received signal power is approximately constant along the two different receivers, which is a typical feature of cylindrical scatterers. We measure a SNR of 31.2 dB in a) and 27.3 dB in b), where the slightly lower SNR in b) is apparent from the noise-floor. Some additional clutter is also present in b), which originates from self-interference or multipath components. A good localization in the range-Doppler domain is observed, indicating that the receivers are phase coherent with the transmitters. Note that the center-locations are approximately the same in range, despite the channels not being timing-offset compensated. This indicates that the communication protocol manages to achieve a synchronization to an order of the inverse bandwidth.

In the considered setup, the Doppler shifts are expected to vary significantly due to variations in aspect angles along the array. This effect can be observed by inspecting the center-location in the Doppler dimension in Fig. 7. As discussed Section III-A, the consequence is that a four-dimensional search might be required in order to capture the velocity components in the matched filter implementation. However, for our considered scenario, there is still a substantial overlap observed, which indicates that the Doppler shifts can be considered approximately constant, and hence alleviating the computational burden. For higher velocities, the overlap is expected to decrease as indicated by (5)-(6).

We conclude that the testbed works well for range-Doppler imaging, and proceed to characterize the localization performance when combining all channels.

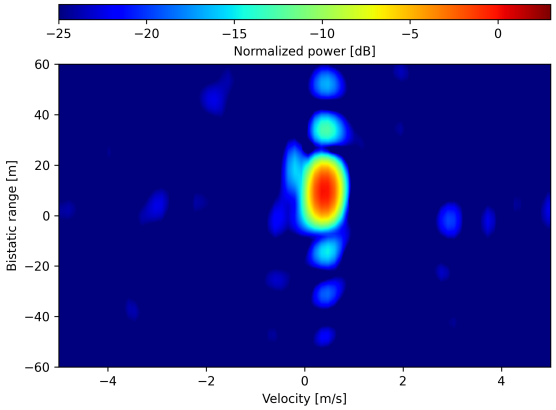

(a) Receiver 1, transmitter 1

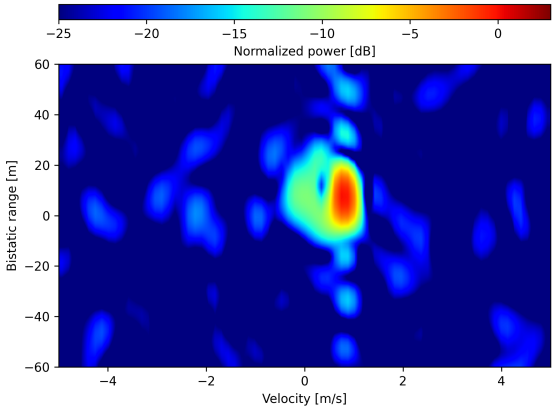

(b) Receiver 64, transmitter 1

Figure 7: Experimental range-Doppler maps of a moving cylinder obtained from the testbed.

B. Coherent transmit-receive combining

Next, we evaluate the localization performance when coherently combining all of the transmit-receive channels. We use two methods for localization, the non-coherent backprojection in (16), and the constant Doppler backprojection in (17). In contrast to the ambiguity function (19), we refer to the matched filter output of a single scatterer in the experimental data as the point spread function (PSF).

A comparison between the ambiguity function and the measured PSFs when using RF absorbers is illustrated in Fig. 8. In order to provide the most realistic (or pessimistic) results, the PSFs have been formed on a cylinder location far away from the measurements used for calibration. Furthermore, only 160 symbols were integrated in the non-coherent backprojection in order to provide an illustrative response similar to the ambiguity function (in practice there is some additional spread due to cell-migration).

As can be seen, the ambiguity function and the PSFs are similar, providing a resolution in the order of few decimeters in the near-field scenario, effectively surpassing the range resolution set by the OFDM bandwidth. It is also observed that the experimental PSFs are slightly distorted when compared to the theoretical ambiguity function. We observed in our measurements (not shown in the paper) that the closer to the calibration points used, the more ideal the PSFs look, and the further away the more distorted they become. This indicates residual errors remaining in system calibration, and is most likely due to the coarsely measured antenna positions, keeping in mind that each antenna position must be known to within a fraction of the wavelength in order for a single point calibration to work everywhere. We recognize this problem of calibrating the array to be a significant challenge in practical settings.

By comparing the non-coherent backprojection with the constant Doppler backprojection, it can be seen that there is additional clutter present in the former PSF. This is because the non-coherent backprojection forms the spatial map with no isolation in Doppler, whereas the latter method isolates the scatterers of interest by processing in a specific Doppler bin.

The empirical cumulative distribution functions (CDFs) in

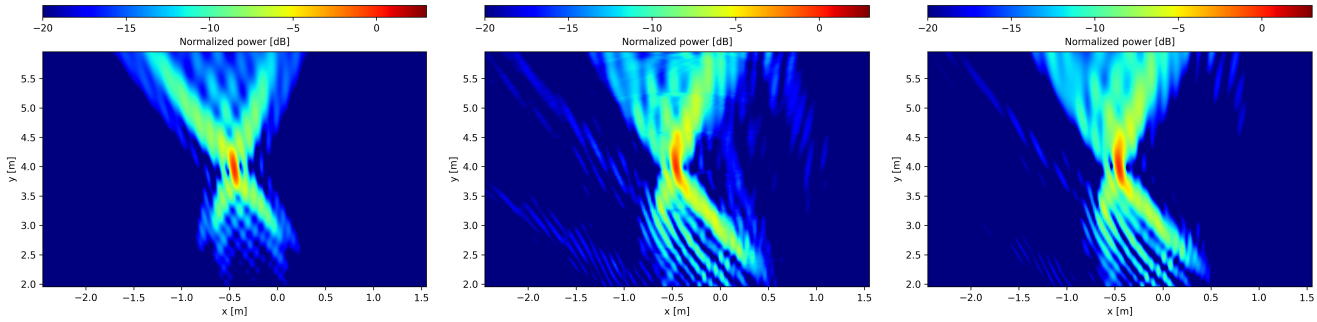

(a) Theoretical ambiguity function (b) Non-coherent backprojection (c) Constant-Doppler backprojection

Figure 8: The (a) spatial ambiguity function and (b)-(c) experimental PSFs evaluated at full bandwidth. The measured PSFs are slightly distorted, which is most likely due to residual calibration errors in antenna locations and gain-phase parameters. The closer to the calibration points used, the more ideal the PSFs look, and the further away the more distorted they become. This indicates the residual errors in signal calibration, and is most likely due to the coarsely measured antenna positions. The clutter is a combination sidelobes originating from the cylinder, multipath components and possibly external interference.

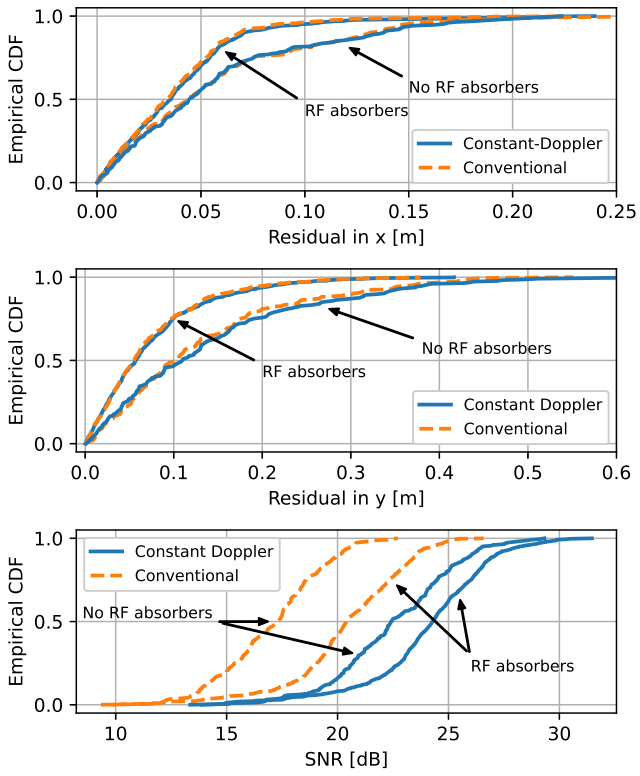

Figure 9: Experimental localization results when coherently combining the transmit-receive channels. It is observed that the location errors are in the order of centimeters to decimeters.

x, y and SNR are illustrated in Fig. 9. The results are illustrated for both with and without RF absorbers. It can be seen that the performance in x and y is nearly identical for both processing approaches, indicating that the constant-Doppler assumption is valid even though the array is widely distributed with respect to the cylinder. It is expected that the performance will degrade further if the scatterer moves faster. Furthermore, we notice a drop in performance when removing the RF absorbers, which is due to the increasing amount of multipath. Interestingly, both methods also perform equally well in terms of localization performance without RF absorbers. The results are summarized in Table II. Without absorbers, the accuracy is measured at 15.6 cm in x and 37 cm in y, as obtained from the 95:th percentiles. With absorbers, the corresponding accuracy is measured at 9.2 cm in x and 20.8 cm in y. The corresponding median errors are 3.4 cm in x and 5.6 cm in y when using absorbers, and 4.4 cm in x and 10.6 cm in y when not using absorbers.

In contrast to the location performance, the algorithms show different performance in the CDFs of the SNRs, where the range-Doppler backprojection provides better performance than the non-coherent backprojection. As illustrated in Fig. 9, the estimated SNR is larger for the constant Doppler backprojection, both with and without RF absorbers, than for the non-coherent backprojection. The difference in performance can be explained by noting that the processing seeks to resolve multiple scatterers in a single range-bin. In this context, the Doppler processing has the advantage of providing a coherent processing gain *and* isolating moving scatterers from clutter and interference. On the other hand, integrating the backprojection non-coherently from symbol to symbol makes less assumptions on the Doppler, but provides only a non-coherent processing gain, in addition to not harnessing the Doppler as a resolving dimension. This explains the difference in performance.

It is worth noting that the SNR is smaller in the spatial maps in Fig. 8 than in the range-Doppler maps (cf. the results in Section VI-A), which indicates that the dominant noise source in the spatial domain is clutter (in this context, we refer to clutter as everything that is not the scatterer of interest, which may be a combination of sidelobes, adjacent scatterers, multipath components or possibly external interference).

We conclude that accurate location estimates can be obtained using the massive MIMO testbed. As shown in Table II, the localization accuracy is on the order of centimeters to

Table II: Error statistics derived from Fig. 9.

RF absorbers	Median	95:th percentile	Unit
Absolute error in x	3.4	9.2	cm
Absolute error in y	5.6	20.8	cm
No RF absorbers			
Absolute error in x	4.4	15.6	cm
Absolute error in y	10.6	37.4	cm

a few decimeters. The PSFs indicate that a relatively good resolution can be obtained in x and y, despite the poor range-resolution. However, we recognize a relatively poor dynamic range as indicated by the heavy skirts in Fig. 8.

C. Effect of using fewer subcarriers

We will now illustrate the effect of using fewer subcarriers and hence a smaller bandwidth than what is achievable in the testbed. The experimental results are illustrated in Fig. 10, where the errors in x and y, and SNR are evaluated against the number of subcarriers when using RF absorbers and the constant Doppler processing in (17). It is observed that the performance remains constant for all considered bandwidths, even when only a single subcarrier is used. This indicates that for the considered scenario, almost all gains in performance originate from the coherent combining of the transmit-receive channels. We note that for 100 subcarriers, a coherent processing gain of 20 dB is to be expected when compared with only a single subcarrier. However, the measured SNR in the spatial map is only 23 dB, which is less than what is obtained in the range-Doppler maps prior to the localization (see Section VI-A). Furthermore, the absence of a performance drop is consistent with the behavior of the CRLBs at fixed SNR in Fig. 6, which indicates that the scenario is indeed clutter limited. This is a reasonable observation given the small bandwidth of the system (i.e, the experimental setup is mapped into the first range bin), and since non-fluctuating clutter experiences the same processing gains as any other scatterers. Therefore, reducing the bandwidth does not degrade the performance any further since the limiting noise in the spatial domain is clutter, and since there are few additional scatterers to "unresolve" when degrading the range-resolution.

As previously mentioned, the symbols have been decimated by a factor of five, giving an effective PRI of 2.5 ms, and thus reducing the maximum unambiguous velocity to ± 17.1 m/s (cf. (24) and Table I). Since it is unexpected for scatterers to move fast in a short-range and indoor environment, we recognize that one may operate the system using less time-frequency resources. For instance, given that the processing gains can be compensated for, the same performance can be obtained by transmitting only 1 subcarrier every 5 ms (giving a maximum unambiguous velocity of 8.7 m/s). This implies that one may operate the radar system in time-division with the communication system with only a nominal loss in spectral efficiency. For the considered scenario, the symbol duration is 71.88 µs, which implies a capacity loss of only 2.87% when operating at a PRI of 2.5 ms, or 1.4% when the PRI is 5 ms. By increasing the subcarrier spacing, one may reduce symbol duration further, and hence also the loss in capacity.

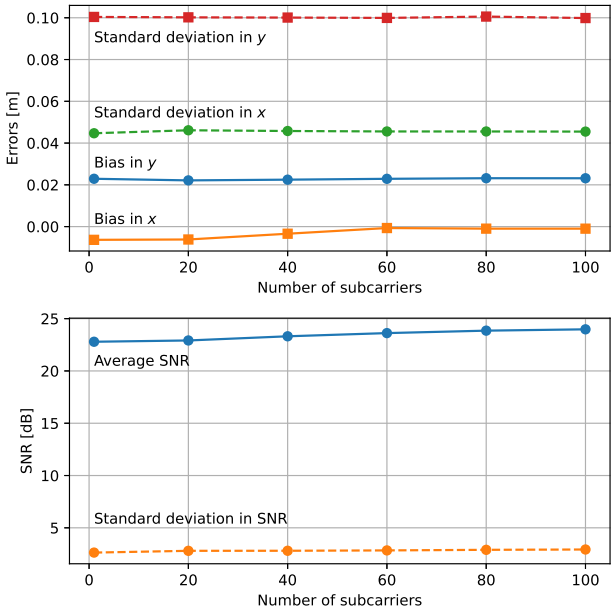

Figure 10: Effect of reducing the number of subcarriers in the experimental setup, using absorbers and range-Doppler processing.

We conclude that only a modest number of subcarriers are needed for localizing the cylinder in the considered setup. This is because of the short-range and near-field scenario, and because most of the performance originates from the large array.

D. Effect of using fewer antennas

We will now evaluate the effect of using fewer antennas when combining the transmit-receive channels. This is done by estimating the location errors obtained from subarrays formed from the receiving and transmitting arrays, each being unambiguously placed. The subarrays are formed by splitting the transmitters and receivers in powers of two, from where the localization errors are calculated separately and then merged for a total assessment.

The results are illustrated in Fig. 11, using the constant Doppler backprojection, where it can be seen that the performance improves with the number of antennas used, both with and without RF absorbers. In contrast to the results in Section VI-C, where the performance was evaluated against the number of subcarriers, it can be seen that the performance is highly affected by the number of antennas. Interestingly, there is a substantial gain in SNR observed, being approximately 9 dB per decade of MIMO channels, until flattening out at around 100 channels. These gains may be attributed to either the coherent processing gains, suppressing the thermal noise, or from the increase in resolution, which reduces the impact of clutter. From the previous discussions, and since the SNR in the spatial map is significantly smaller than in the range-Doppler maps in Section VI-A, we make the conclusion that it is due to the increase in resolution.

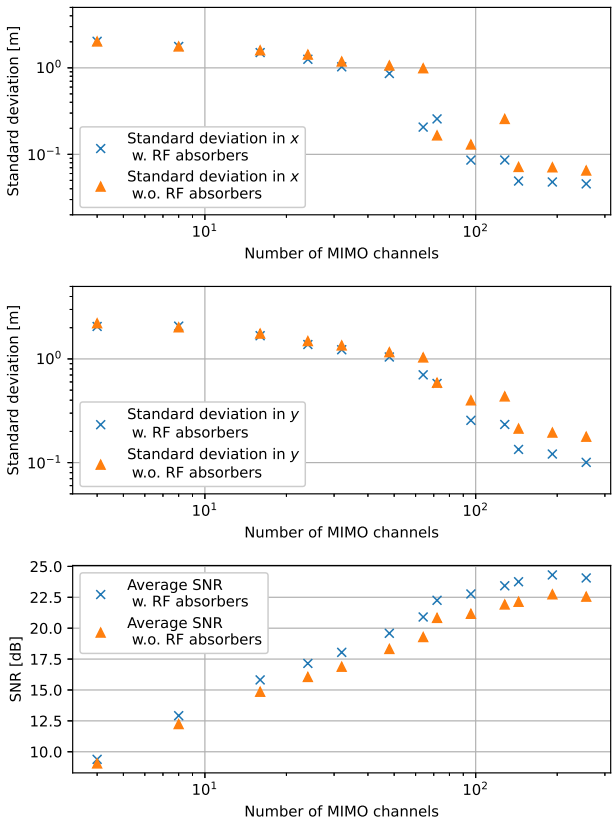

Figure 11: Effect on localization performance when using fewer antennas at unambiguous spacing.

We conclude that in order to compensate for the lack of bandwidth, a large number of antennas (in the case considered, corresponding to >100 channels) are needed, which is well suited within the massive MIMO communications paradigm.

VII. Conclusion

This paper has presented an analysis of near-field sensing using a massive MIMO communication testbed utilizing the OFDM waveform. The testbed was re-used for radar sensing by processing the CSI and taking advantage of the large number of antennas. The performance was evaluated numerically, showing feasibility in the considered near-field environment. The numerical results were validated with experimental measurements, and it was demonstrated that centimeter level accuracy is achievable even under dense indoor multipath, and that the Doppler dimension provides valuable performance gains in clutter-limited environments. With RF absorbers, a median error of 3.5 cm in x and 5.5 cm in y was measured. Without absorbers, the corresponding errors were measured to 9 cm in x and 21 cm in y.

It was shown numerically (with the ambiguity function and the CRLB), and experimentally (with the testbed), that practically no bandwidth is needed in the near-field of the considered array. When the aspect angles are sufficiently diverse, the array resolution dominates the localization performance. Furthermore, it was shown that the radar system can be operated with an effective transmission period of one symbol per 2.5 ms, which allows for a time division multiplexing between the communication and radar functionalities with only a nominal loss in spectral efficiency, corresponding to a 2.87% capacity loss at a symbol duration of 71.88 µs. The performance was also evaluated against the number of transmitters and receivers, where it was observed that the performance depends strongly on the number of antennas used. The results show that massive MIMO communication systems may provide an opportunity for accurate radar sensing in the near-field, even with the small bandwidths encountered at low carrier frequencies.

We recognize several aspects that need to be considered in future research. This includes a further investigation of the matched filter approximations, the impact of different antenna distributions and the effect of transceiver non-idealities. Reliable calibration schemes, and carrier and clock synchronization algorithms are considered as enabling, and scenarios with multiple complex scatterers should be studied properly in order to analyze the dynamic range and the feasibility of the constant amplitude assumption.

Appendix A

Derivation of the CRLB in (18)

For a single point scatterer, and letting $\dot{d}_{mn} = 0$ and $\alpha_{mn} \approx \alpha = |\alpha|e^{j\phi}$, the signal model becomes

$$x_{mn}(k,l) = |\alpha| e^{j\phi} e^{-j2\pi\left(\frac{1}{\lambda}+\frac{\Delta f}{c}k\right)d_{mn}}. \tag{30}$$

The parameter vector is $\boldsymbol{\gamma} = [|\alpha|, \phi, x, y]^T$. The FIM is obtained via the Slepian-Bangs formula [46], [54] as

$$\boldsymbol{F}_{mnkl}(x,y) = \frac{1}{\sigma}\text{Re}\left\{\left(\frac{dx_{mn}(k,l)}{d\boldsymbol{\gamma}}\right)\left(\frac{dx_{mn}(k,l)}{d\boldsymbol{\gamma}}\right)^H\right\}. \tag{31}$$

Since the noise and space-time snapshots are assumed white and independent, and since $x_{mn}(k,l)$ does not depend on l, the total FIM is obtained as

$$\boldsymbol{F}(x,y) = \frac{1}{L}\sum_{m=1}^{M}\sum_{n=1}^{N}\sum_{k=1}^{K}\boldsymbol{F}_{mnk}(x,y), \tag{32}$$

where $\boldsymbol{F}_{mnk}(x,y) = \boldsymbol{F}_{mnkl}(x,y)$. We have $\frac{dx_{mn}(k,l)}{d\boldsymbol{\gamma}} = [\frac{dx_{mn}(k,l)}{d|\alpha|}, \frac{dx_{mn}(k,l)}{d\phi}, \frac{dx_{mn}(k,l)}{dx}, \frac{dx_{mn}(k,l)}{dy}]^T$, where

$$\frac{dx_{mn}(k,l)}{d|\alpha|} = e^{j\phi}e^{-j2\pi\left(\frac{1}{\lambda}+\frac{\Delta f}{c}k\right)d_{mn}} \tag{33}$$

$$\frac{dx_{mn}(k,l)}{d\phi} = jx_{mn}(k,l) \tag{34}$$

$$\frac{dx_{mn}(k,l)}{dx} = -j2\pi\left(\frac{1}{\lambda}+\frac{\Delta f}{c}k\right)\frac{dd_{mn}}{dx}x_{mn}(k,l) \tag{35}$$

$$\frac{dx_{mn}(k,l)}{dy} = -j2\pi\left(\frac{1}{\lambda}+\frac{\Delta f}{c}k\right)\frac{dd_{mn}}{dy}x_{mn}(k,l) \tag{36}$$

where $\frac{\mathrm{d}d_{mn}}{\mathrm{d}x} = \frac{x-x_m}{d_m} + \frac{x-x_n}{d_n}$ and $\frac{\mathrm{d}d_{mn}}{\mathrm{d}y} = \frac{y-y_m}{d_m} + \frac{y-y_n}{d_n}$. The CRLB is obtained numerically as

$$\text{CRLB}(x,y) = \boldsymbol{F}(x,y)^{-1}. \tag{37}$$

Derivation of the CRLBs δd_{mn} and $\delta \dot{d}_{mn}$ in Section III-B

From equation (10) in [55], it can be shown that the CRLB in bistatic range is

$$\delta d_{mn}^2 = \frac{6\sigma^2}{\pi^2(\Delta f/c)^2 \alpha_{mn}^2 K(K^2-1)L}. \tag{38}$$

By assuming that $K^2 - 1 \approx K^2$, and substituting in (21) and (27), we get $\delta d_{mn}^2 \approx \frac{3\Delta d^2}{\pi^2 \mathrm{SNR}_{mn}}$, which gives

$$\delta d_{mn} \approx \frac{\Delta d}{\sqrt{\pi \mathrm{SNR}_{mn}}}. \tag{39}$$

Similarly, it can easily be shown that $\delta \dot{d}_{mn}$ can be approximated by the expression in (26).

REFERENCES

[1] M. Shafi, A. F. Molisch, P. J. Smith, T. Haustein, P. Zhu, P. D. Silva, F. Tufvesson, A. Benjebbour, and G. Wunder, "5G: A Tutorial Overview of Standards, Trials, Challenges, Deployment, and Practice," *IEEE Journal on Selected Areas in Communications*, vol. 35, no. 6, pp. 1201–1221, jun 2017.

[2] N. Rajatheva, I. Atzeni, E. Björnson, A. Bourdoux, S. Buzzi, J.-B. Dore, S. Erkucuk, M. Fuentes, K. Guan, Y. Hu, X. Huang, J. Hulkkonen, J. M. Jornet, M. Katz, R. Nilsson, E. Panayirci, K. Rabie, N. Rajapaksha, M. Salehi, H. Sarieddeen, T. Svensson, O. Tervo, A. Tolli, Q. Wu, and W. Xu, "White Paper on Broadband Connectivity in 6G," https://arxiv.org/abs/2004.14247.

[3] N. Rajatheva, I. Atzeni, S. Bicais, E. Björnson, A. Bourdoux, S. Buzzi, C. D'Andrea, J.-B. Dore, S. Erkucuk, M. Fuentes, K. Guan, Y. Hu, X. Huang, J. Hulkkonen, J. M. Jornet, M. Katz, B. Makki, R. Nilsson, E. Panayirci, K. Rabie, N. Rajapaksha, M. Salehi, H. Sarieddeen, S. Shahabuddin, T. Svensson, O. Tervo, A. Tolli, Q. Wu, and W. Xu, "Scoring the terabit/s goal:broadband connectivity in 6g," https://arxiv.org/abs/2008.07220.

[4] H. Tataria, M. Shafi, A. F. Molisch, M. Dohler, H. Sjöland, and F. Tufvesson, "6G Wireless Systems: Vision, Requirements, Challenges, Insights, and Opportunities," *Proceedings of the IEEE*, pp. 1–34, 2021.

[5] J. A. Zhang, F. Liu, C. Masouros, R. W. H. Jr., Z. Feng, L. Zheng, and A. Petropulu, "An Overview of Signal Processing Techniques for Joint Communication and Radar Sensing," Feb. 2021, https://arxiv.org/abs/2102.12780.

[6] S. H. Dokhanchi, B. S. Mysore, K. V. Mishra, and B. Ottersten, "A mmWave Automotive Joint Radar-Communications System," *IEEE Transactions on Aerospace and Electronic Systems*, vol. 55, no. 3, pp. 1241–1260, 2019.

[7] K. V. Mishra, M. B. Shankar, V. Koivunen, B. Ottersten, and S. A. Vorobyov, "Toward Millimeter-Wave Joint Radar Communications: A Signal Processing Perspective," *IEEE Signal Processing Magazine*, vol. 36, no. 5, pp. 100–114, sep 2019.

[8] D. Ma, N. Shlezinger, T. Huang, Y. Liu, and Y. C. Eldar, "Joint radar-communication strategies for autonomous vehicles: Combining two key automotive technologies," *IEEE Signal Processing Magazine*, vol. 37, no. 4, pp. 85–97, jul 2020.

[9] M. L. Rahman, J. A. Zhang, X. Huang, Y. J. Guo, and R. W. Heath, "Framework for a Perceptive Mobile Network Using Joint Communication and Radar Sensing," *IEEE Transactions on Aerospace and Electronic Systems*, vol. 56, no. 3, pp. 1926–1941, 2020.

[10] J. A. Zhang, M. L. Rahman, K. Wu, X. Huang, Y. J. Guo, S. Chen, and J. Yuan, "Enabling Joint Communication and Radar Sensing in Mobile Networks – A Survey," 2021, https://arxiv.org/abs/2006.07559.

[11] L. Zheng, M. Lops, Y. C. Eldar, and X. Wang, "Radar and Communication Coexistence: An Overview: A Review of Recent Methods," *IEEE Signal Processing Magazine*, vol. 36, no. 5, pp. 85–99, sep 2019.

[12] F. Liu, C. Masouros, A. Li, H. Sun, and L. Hanzo, "MU-MIMO Communications With MIMO Radar: From Co-Existence to Joint Transmission," *IEEE Transactions on Wireless Communications*, vol. 17, no. 4, pp. 2755–2770, apr 2018.

[13] A. Hassanien, M. G. Amin, E. Aboutanios, and B. Himed, "Dual-Function Radar Communication Systems: A Solution to the Spectrum Congestion Problem," *IEEE Signal Processing Magazine*, vol. 36, no. 5, pp. 115–126, 2019.

[14] F. Liu, C. Masouros, A. P. Petropulu, H. Griffiths, and L. Hanzo, "Joint Radar and Communication Design: Applications, State-of-the-Art, and the Road Ahead," *IEEE Transactions on Communications*, vol. 68, no. 6, pp. 3834–3862, jun 2020.

[15] N. C. Luong, X. Lu, D. T. Hoang, D. Niyato, and D. I. Kim, "Radio Resource Management in Joint Radar and Communication: A Comprehensive Survey," *IEEE Communications Surveys Tutorials*, vol. 23, no. 2, pp. 780–814, 2021.

[16] T. L. Marzetta, "Noncooperative Cellular Wireless with Unlimited Numbers of Base Station Antennas," *IEEE Transactions on Wireless Communications*, vol. 9, no. 11, pp. 3590–3600, nov 2010.

[17] E. Björnson, L. Sanguinetti, H. Wymeersch, J. Hoydis, and T. L. Marzetta, "Massive MIMO is a Reality – What is Next? Five Promising Research Directions for Antenna Arrays," Feb. 2019, https://arxiv.org/abs/1902.07678.

[18] B. M. Lee and H. Yang, "Massive MIMO With Massive Connectivity for Industrial Internet of Things," *IEEE Transactions on Industrial Electronics*, vol. 67, no. 6, pp. 5187–5196, 2020.

[19] D. Ciuonzo, P. S. Rossi, and S. Dey, "Massive MIMO Channel-Aware Decision Fusion," *IEEE Transactions on Signal Processing*, vol. 63, no. 3, pp. 604–619, 2015.

[20] A. Haimovich, R. Blum, and L. Cimini, "MIMO radar with widely separated antennas," *IEEE Signal Processing Magazine*, vol. 25, no. 1, pp. 116–129, 2008.

[21] S. Fortunati, L. Sanguinetti, F. Gini, M. S. Greco, and B. Himed, "Massive MIMO Radar for Target Detection," *IEEE Transactions on Signal Processing*, vol. 68, pp. 859–871, 2020.

[22] C. Baquero Barneto, T. Riihonen, M. Turunen, L. Anttila, M. Fleischer, K. Stadius, J. Ryynänen, and M. Valkama, "Full-Duplex OFDM Radar With LTE and 5G NR Waveforms: Challenges, Solutions, and Measurements," *IEEE Transactions on Microwave Theory and Techniques*, vol. 67, no. 10, pp. 4042–4054, 2019.

[23] S. D. Liyanaarachchi, C. B. Barneto, T. Riihonen, and M. Valkama, "Experimenting Joint Vehicular Communications and Sensing with Optimized 5G NR Waveform," in *2021 IEEE 93rd Vehicular Technology Conference (VTC2021-Spring)*, 2021, pp. 1–5.

[24] C. B. Barneto, S. D. Liyanaarachchi, M. Heino, T. Riihonen, and M. Valkama, "Full Duplex Radio/Radar Technology: The Enabler for Advanced Joint Communication and Sensing," *IEEE Wireless Communications*, vol. 28, no. 1, pp. 82–88, 2021.

[25] Q. Zhang, X. Wang, Z. Li, and Z. Wei, "Design and Performance Evaluation of Joint Sensing and Communication Integrated System for 5G MmWave Enabled CAVs," *IEEE Journal of Selected Topics in Signal Processing*, pp. 1–1, 2021.

[26] P. Kumari, A. Mezghani, and R. W. Heath, "JCR70: A Low-Complexity Millimeter-Wave Proof-of-Concept Platform for a Fully-Digital SIMO Joint Communication-Radar," *IEEE Open Journal of Vehicular Technology*, vol. 2, pp. 218–234, 2021.

[27] G. Interdonato, E. Björnson, H. Q. Ngo, P. Frenger, and E. G. Larsson, "Ubiquitous cell-free Massive MIMO communications," *EURASIP Journal on Wireless Communications and Networking*, vol. 2019, no. 1, aug 2019.

[28] E. Björnson and L. Sanguinetti, "Scalable Cell-Free Massive MIMO Systems," *IEEE Transactions on Communications*, vol. 68, no. 7, pp. 4247–4261, 2020.

[29] F. Liu, L. Zhou, C. Masouros, A. Li, W. Luo, and A. Petropulu, "Toward Dual-functional Radar-Communication Systems: Optimal Waveform Design," *IEEE Transactions on Signal Processing*, vol. 66, no. 16, pp. 4264–4279, 2018.

[30] C. Sturm and W. Wiesbeck, "Waveform design and signal processing aspects for fusion of wireless communications and radar sensing," *Proceedings of the IEEE*, vol. 99, no. 7, pp. 1236–1259, jul 2011.

[31] K. M. Braun, "OFDM Radar Algorithms in Mobile Communication Networks," Ph.D. dissertation, 2014.

[32] N. H. Lehmann, A. M. Haimovich, R. S. Blum, and L. Cimini, "High resolution capabilities of MIMO radar," in *2006 Fortieth Asilomar Conference on Signals, Systems and Computers*. IEEE, 2006.

[33] E. Fishler, A. Haimovich, R. Blum, L. Cimini, D. Chizhik, and R. Valenzuela, "Spatial diversity in radars—models and detection performance," *IEEE Transactions on Signal Processing*, vol. 54, no. 3, pp. 823–838, mar 2006.

[34] J. Li, P. Stoica, L. Xu, and W. Roberts, "On parameter identifiability of MIMO radar," *IEEE Signal Processing Letters*, vol. 14, no. 12, pp. 968–971, dec 2007.

[35] J. Li and P. Stoica, "MIMO radar with colocated antennas," *IEEE Signal Processing Magazine*, vol. 24, no. 5, pp. 106–114, sep 2007.

[36] P. Stoica, J. Li, and Y. Xie, "On probing signal design for MIMO radar," *IEEE Transactions on Signal Processing*, vol. 55, no. 8, pp. 4151–4161, aug 2007.

[37] L. Xu, J. Li, and P. Stoica, "Target detection and parameter estimation for MIMO radar systems," *IEEE Transactions on Aerospace and Electronic Systems*, vol. 44, no. 3, pp. 927–939, jul 2008.

[38] D. Kirk, J. Bergin, P. Techau, and J. Carlos, "Multi-static coherent sparse aperture approach to precision target detection and engagement," in *IEEE International Radar Conference, 2005.* IEEE, 2005.

[39] A. Dogandzic and A. Nehorai, "Cramer-Rao bounds for estimating range, velocity, and direction with an active array," *IEEE Transactions on Signal Processing*, vol. 49, no. 6, pp. 1122–1137, jun 2001.

[40] M. Lipka, S. Brückner, E. Sippel, and M. Vossiek, "On the Needlessness of Signal Bandwidth for Precise Holographic Wireless Localization," in *2020 17th European Radar Conference (EuRAD)*, 2021, pp. 202–205.

[41] Z. Chen and E. Björnson, "Channel Hardening and Favorable Propagation in Cell-Free Massive MIMO With Stochastic Geometry," *IEEE Transactions on Communications*, vol. 66, no. 11, pp. 5205–5219, 2018.

[42] M. A. Richards, J. A. Scheer, and W. A. Holm, Eds., *Principles of Modern Radar: Basic principles*. Institution of Engineering and Technology, jan 2010.

[43] M. Richards, *Fundamentals of Radar Signal Processing, Second Edition*. McGraw-Hill Education, 2014.

[44] B. Friedlander, "Localization of Signals in the Near-Field of an Antenna Array," *IEEE Transactions on Signal Processing*, vol. 67, no. 15, pp. 3885–3893, 2019.

[45] A. V. Oppenheim and R. W. Schafer, *Discrete-Time Signal Processing*. Pearson, 2009.

[46] P. Stoica, *Spectral analysis of signals*. Upper Saddle River, N.J: Pearson/Prentice Hall, 2005.

[47] "LabVIEW Communications MIMO Application Framework 1.5," March 2021, [Online] https://download.ni.com/evaluation/rf/MIMO_Application_Framework_Manual_ver_1.5.pdf.

[48] C.-M. Chen, S. Blandino, A. Gaber, C. Desset, A. Bourdoux, L. V. der Perre, and S. Pollin, "Distributed massive MIMO: A diversity combining method for TDD reciprocity calibration," in *GLOBECOM 2017 - 2017 IEEE Global Communications Conference*. IEEE, dec 2017.

[49] L. Monteyne, A. P. Guevara, G. Callebaut, S. Gunnarsson, L. V. der Perre, and S. Pollin, "Matrix pencil method: Angle of arrival and channel estimation for a massive MIMO system," in *ICC 2020 - 2020 IEEE International Conference on Communications (ICC)*. IEEE, jun 2020.

[50] Y. Pan, S. De Bast, and S. Pollin, "Indoor Direct Positioning With Imperfect Massive MIMO Array Using Measured Near-Field Channels," *IEEE Transactions on Instrumentation and Measurement*, vol. 70, pp. 1–11, 2021.

[51] C.-M. Chen, V. Volski, L. V. der Perre, G. A. E. Vandenbosch, and S. Pollin, "Finite Large Antenna Arrays for Massive MIMO: Characterization and System Impact," *IEEE Transactions on Antennas and Propagation*, vol. 65, no. 12, pp. 6712–6720, dec 2017.

[52] A. Molisch, *Wireless Communications*. John Wiley & Sons, 2010.

[53] F. Harris, "On the use of windows for harmonic analysis with the discrete Fourier transform," *Proceedings of the IEEE*, vol. 66, no. 1, pp. 51–83, 1978.

[54] S. M. Kay, *Fundamentals of Statistical Signal Processing: Estimation Theory*. USA: Prentice-Hall, Inc., 1993.

[55] A. Sakhnini, M. Guenach, A. Bourdoux, and S. Pollin, "A Cramér-Rao Lower Bound for Analyzing the Localization Performance of a Multistatic Joint Radar-Communication System," in *2021 1st IEEE International Online Symposium on Joint Communications & Sensing (JC&S) (JC&S'21)*, Feb. 2021.